# Iron-alumina composites: From discrete iron particles to interconnected iron network. Powder synthesis, spark plasma sintering, microstructure and mechanical properties

Christophe Laurent, David Mesguich, Laura Séverac, Rainui Tetihia, Geoffroy Chevallier, Claude Estournès

Open Ceramics 16 (2023) 100485

Contents lists available at ScienceDirect

Open Ceramics

journal homepage: www.sciencedirect.com/journal/open-ceramics

# Iron-alumina composites: From discrete iron particles to interconnected iron network. Powder synthesis, spark plasma sintering, microstructure and mechanical properties

Christophe Laurent [a,*], David Mesguich [a], Laura Séverac [a], Rainui Tetihia [a], Geoffroy Chevallier [a,b], Claude Estournès [a]

[a] CIRIMAT, Université Toulouse 3 Paul Sabatier, Toulouse INP, CNRS, Université de Toulouse, 118 route de Narbonne, 31062, Toulouse, cedex 9, France
[b] Plateforme Nationale CNRS de Frittage Flash, PNF2, Université Toulouse 3 Paul Sabatier, CNRS, Université de Toulouse, 118 route de Narbonne, 31062, Toulouse, cedex 9, France

ARTICLE INFO

Handling Editor: Dr Catherine Elissalde

*Keywords:*
Composites
Iron
Alumina
Spark plasma sintering
Mechanical properties

ABSTRACT

The aim is to prepare Fe–$Al_2O_3$ ceramic-matrix composites with a high Fe content in order to benefit from a high degree of toughening. Fe–$Al_2O_3$ powders with different Fe contents (14.2–47.4 vol%) are prepared by selective reduction in $H_2$ of the corresponding amorphous $Al_{2-2x}Fe_{2x}O_3$ oxides, themselves prepared by decomposition in air of the mixed oxalates. Dense samples are prepared by Spark Plasma Sintering. The samples are investigated by thermal analysis, scanning electron microscopy and X-ray diffraction. The microhardness, fracture strength and toughness are discussed with respect to the composition and the microstructure, i.e. a dispersion of discrete Fe particles or a continuous Fe network into the alumina matrix. The latter samples are significantly thougher than the former ones (about 14 and 8 MPa $m^{1/2}$, respectively).

## 1. Introduction

Composite materials consisting of a dispersion of metallic particles in a ceramic matrix have been the subject of studies for several decades [1,2], notably regarding toughening [3–6]. Iron-alumina (Fe–$Al_2O_3$) composites have been investigated in this respect [7–21] and interesting electrical and magnetic properties [22–30] have also been highlighted. Iron has many advantages over other metals (chromium, cobalt, nickel, molybdenum, niobium, silver, …), including availability, price and inocuity. Its potential for oxidation obviously introduces some limitations for use at high temperatures, but the possibility of forming compounds such as $Fe_2O_3$, $Fe_3O_4$ and $FeAl_2O_4$ also opens up certain functional possibilities such as a tunable negative permittivity and permeability [27,28]. The toughness is expected to increase upon the increase in metal content in the composite [31] but many factors are to be considered, including the metal particle size distribution, the strength of the metal-matrix interface, the ability of a metal particle to deform plastically and the matrix grain size refinement induced by he presence of the metal particles. A schematic representation of the toughness gain *vs* metal content for several microstructures is shown in Fig. 1. The toughening provided by a dispersion of nanometric metal particles within the matrix grains (intragranular nanocomposites) is important but its reaches a plateau for about 2 vol% of metal (red line in Fig. 1) [8,12]. Submicrometer-sized particles located at an increasing proportion of the matrix grain junctions provide a more progressive toughening (blue line in Fig. 1) [31]. However, ultimately there is a metal content for which there is a particle at every grain junction and a further increase may result in an exaggerate growth of the metal particles, leading in practice to a loss of the control of the microstructure and a decreased toughening (decreasing part of the blue line in Fig. 1). It is difficult to avoid this when the proportion of metallic phase exceeds about 20 vol%. A further gain in toughening could be nevertheless be obtained if the appropriate microstructure could be achieved for higher metal contents (dotted green line in Fig. 1) and this is the aim of this paper. The preparation of the composite powder is a key step in ensuring the final homogeneity of the dispersion of the metal into the $Al_2O_3$ matrix. Reported methods involve mixing $Al_2O_3$ and Fe powders, mechanosynthesis (solid-state reduction which occurs during ball-milling of mixtures of $Fe_2O_3$ and Al powders) and routes using $Fe_2O_3$ as Fe precursor, either free or forming a solid solution with $Al_2O_3$. The dense

* Corresponding author.
*E-mail addresses:* christophe.laurent@univ-tlse3.fr (C. Laurent), david.mesguich@univ-tlse3.fr (D. Mesguich), laura.severac@gmail.com (L. Séverac), tetihia@gmail.com (R. Tetihia), geoffroy.chevallier@univ-tlse3.fr (G. Chevallier), claude.estournes@univ-tlse3.fr (C. Estournès).

https://doi.org/10.1016/j.oceram.2023.100485
Received 8 August 2023; Received in revised form 29 September 2023; Accepted 5 October 2023
Available online 6 October 2023

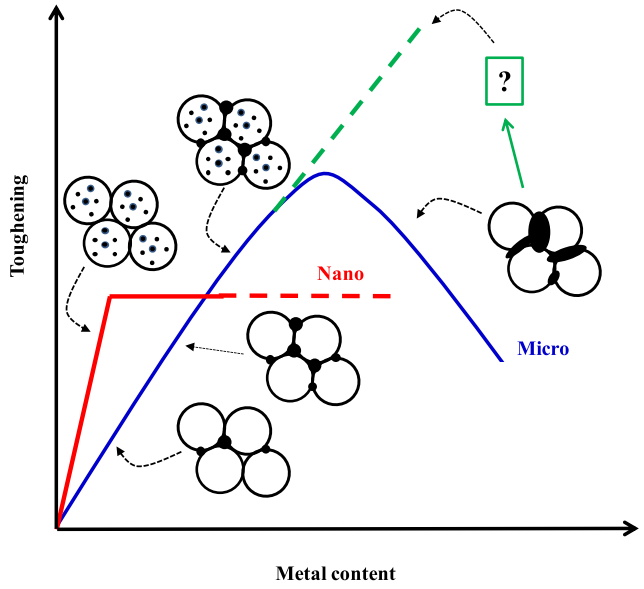


**Fig. 1.** Schematic representation of toughening *vs* metal content for several types of microstructure. "Nano" and the red line represent the toughening originating from intragranular nanometric metal particles. "Micro" and the blue line represent the toughening originating from intergranular (sub)micrometric metal particles. The dotted green line represents the toughening gain that could be obtained if the appropriate microstructure could be achieved.

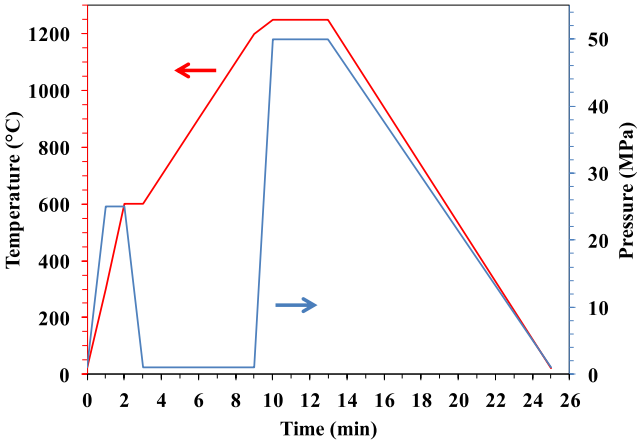


**Fig. 2.** SPS temperature and pressure cycles for all samples except C23S (maximum temperature 1400 °C).

**Table 1**
Proportions of $Fe^{3+}$ relative to ($Fe^{3+}$ + $Al^{3+}$) in the oxide (cat.%) powders and proportions of $Fe^0$ relative to the Fe–$Al_2O_3$ composite powders (mol.%, wt.% and vol%).

| Oxide | $Fe^{3+}$ (cat.%) | Composite | $Fe^0$ (mol.%) | $Fe^0$ (wt.%) | $Fe^0$ (vol%) |
|---|---|---|---|---|---|
| O23 | 23 | C23 | 37.4 | 24.7 | 14.2 |
| O31 | 31 | C31 | 47.3 | 33.0 | 19.9 |
| O42 | 42 | C42 | 59.2 | 44.2 | 28.6 |
| O52 | 52 | C52 | 68.4 | 54.3 | 37.4 |
| O62 | 62 | C62 | 76.5 | 64.1 | 47.4 |

samples are prepared by sintering the Fe–$Al_2O_3$ powders, at temperatures higher than 1300 °C, using usually either hot-pressing (HP) or spark plasma sintering (SPS), the latter method allowing for lower

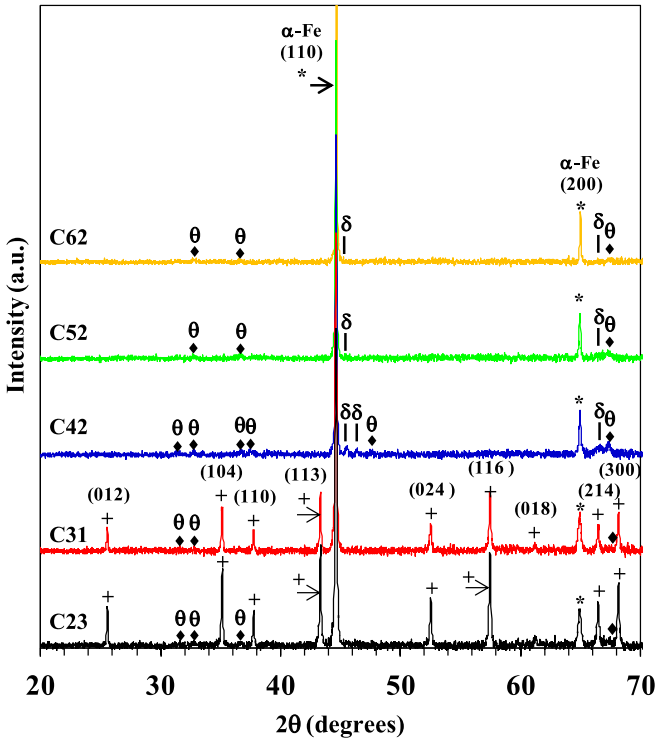


**Fig. 3.** XRD patterns of the C powders. The peaks of a-Fe (*), α-$Al_2O_3$ (+), δ-$Al_2O_3$ (l) and θ-$Al_2O_3$ (◆) are indexed. The patterns are normalized to the α-Fe(110) peak.

temperatures and shorter cycles. Fe–$Al_2O_3$ powders with Fe contents significantly higher than 20 vol% (up to 47 vol%), without an exaggerated growth of the Fe particles are prepared, and densified by SPS. Mechanical characteristics will be presented and discussed in relation to the composition and microstructure.

## 2. Experimental

### 2.1. Synthesis

Powders of ammonium tris-oxalato aluminoferrate with different iron contents, $(NH_4)_3[Al_{1-x}Fe_x(C_2O_4)_3].nH_2O$ (x = 0.23; 0.31; 0.42; 0.52; 0.62), were prepared by the mixed-oxalate precipitation route [32]. The so-obtained oxalates were decomposed by a heat-treatment in air (400 °C, 3 h) in order to form the corresponding amorphous-$(Al_{1-x}Fe_x)_2O_3$ oxides [33]. The oxide powders were reduced in pure $H_2$ in order to obtain Fe–$Al_2O_3$ composite powders in experimental conditions (1100 °C, 5 h) appropriate for the total reduction of the ferric ions into metallic iron [34,35]. The oxides and composites will be denoted hereafter as the O and C powders, respectively. The oxide powders will denoted with an indication of the iron content, for example O42 for the powder with x = 0.42. For the sake of simplicity, the corresponding composite powder will be denoted as C42 although this may give a poor representation of the sample because the x values are not relevant data anymore. This point will be addressed later in the text.

### 2.2. Sintering

The powders were consolidated by SPS (SPS 632LX, Fuji electronic Industrial Co., Japan). The powders (3–3.7 g depending on the iron content) were loaded into a 20 mm inner-diameter graphite die. A sheet of graphitic paper was placed between the punch and the powder and between the die and the powder for easy removal. The samples were sintered in vacuum (residual cell pressure <5 Pa). A direct current with a

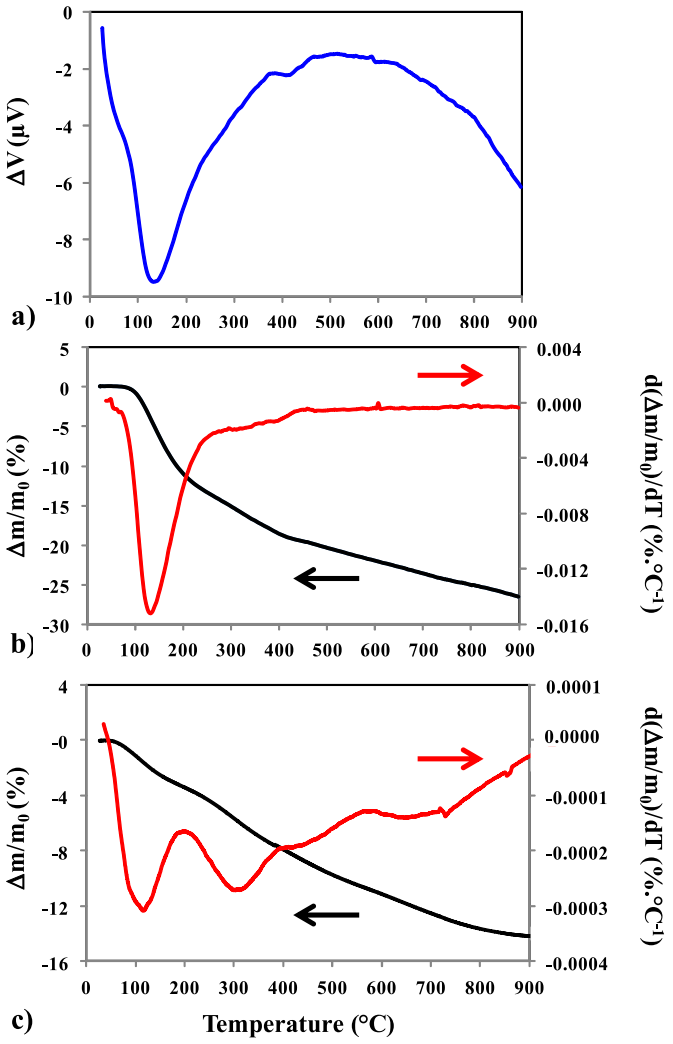


**Fig. 4.** Thermal analysis in flowing $H_2$ of powder O31: a) DTA curve recorded at 20 °C/min; b) TGA curve (black) and DTG (red) curves recorded simultaneously to the DTA; c) TGA curve (black) and DTG (red) curves recorded at 2 °C/min.

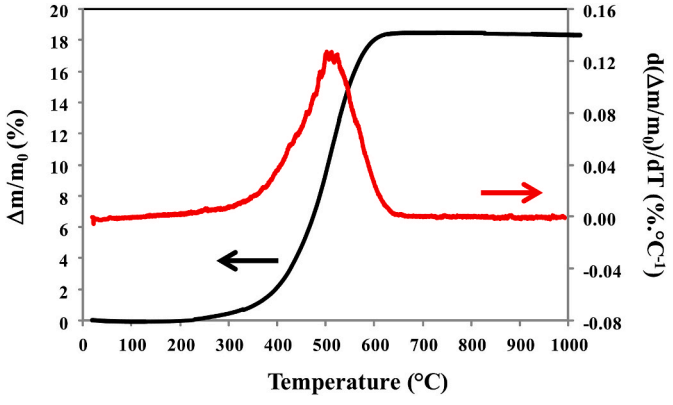


**Fig. 5.** Thermal analysis in flowing air of powder C42: TGA curve (black) and DTG (red) curves.

pulse pattern of 40 ms on: 7 ms off was used. An optical pyrometer, focused on a little hole (3 mm in depth) at the outer surface of the die, was used to control the temperature. The SPS temperature and pressure cycles are summarized in Fig. 2. A heating rate of about 300 °C/min was used from room temperature to 600 °C. The power was automatically and gradually increased until the temperature is detected by the pyrometer at 570 °C (detection threshold), which takes about 2 min. A 1 min dwell time was applied at 600 °C in order to offset any overshoot, which from experience is known to be very minor anyway, and stabilize the temperature of the SPS stack at 600 °C before the start of the controlled ramp. Then, the temperature was raised (100 °C/min) to 1200 °C and to 1250 °C at 50 °C/min to avoid overshoot (1400 °C for C23S), where a 3 min dwell was applied. A uniaxial load corresponding to 25 MPa was gradually applied during the heating to 600 °C and was maintained during the dwell at this temperature. It was decreased to a contact pressure for the heating step up to the dwell, to be raised again during the last minute before the dwell at the maximum temperature and was maintained until the end of the dwell. The corresponding pressure is equal to 50 MPa. A cooling rate of 100 °C/min was applied down to room temperature and the uniaxial load was gradually released during the same time. The sintered specimens were in the form of pellets 20 mm in diameter and about 3 mm thick. The graphitic paper remaining on the surface was removed by polishing. The sintered samples will be denoted hereafter after the corresponding composite powder, adding an S for sintered, i.e. sample C42S, sintered from powder C42.

### 2.3. Characterization

The iron and aluminium content in the O powders were measured by the Inductively Coupled Plasma Mass Spectrometry (ICP-MS) method with an accuracy of ±2 %. The samples were investigated using X-ray diffraction (XRD, Cu $K_\alpha$ radiation, Bruker D4 Endeavor). Thermogravimetric analysis (TGA) and differential thermal analysis (DTA) of selected O powders were performed in a Setaram Setsys Evo module. The powders (7–10 mg) were heated (20 °C/min for DTA and 2 °C/min for TGA) from room temperature to 900 °C in a constant flow of $H_2$ (1.8 L/h). TGA of the C powders was performed in a Setaram TAG 16 module (simultaneous symmetrical thermoanalyser). The powders (7–10 mg) were heated (5 °C/min) from room temperature to 1000 °C in a constant flow of synthetic air (1.5 L/h). The C powders were observed by field-emission-gun scanning electron microscopy (FESEM, JEOL JSM 7800F, operated at 10 kV). The size distribution of the Fe particles on the powders and dense samples was evaluated on FESEM images using image analysis (Image J software). The density of the specimens was measured by Archimedes' method using a hydrostatic balance (Sartorius MSE224S-YDK03) with an accuracy of ±1 %. The relative density was calculated using 7.86 g/cm$^3$ for iron, 3.97 g/cm$^3$ for α-$Al_2O_3$ and 3.95 g/cm$^3$ for the spinel $FeAl_2O_4$.

Tests (500 g, i.e. 4.9 N, for 10 s in air at room temperature) were performed using a Vickers indenter (Mitutoyo HM 2000) on polished transverse sections of the samples (polishing down to 3 μm followed by 0.02 μm colloidal $SiO_2$). The values reported are the average of at least 6 measurements. The transverse fracture strength ($\sigma_f$) was measured, parallel to the SPS pressing axis, by the three-point bending method (Materials Test Systems) on polished ((polishing down to 3 μm followed by 0.02 μm colloidal $SiO_2$) specimens about 1.8 × 1.8 × 18 mm$^3$ The span between the two supporting pins is equal to 13 mm. Cross-head speed was fixed at 0.1 mm/min. The toughness ($K_{Ic}$) was measured, also parallel to the pressing axis, by the single-edged notched beam (SENB) method, on similar specimens notched with a diamond wire 0.17 mm in diameter. The notch depth/height ratio was verified to be slightly higher than 0.4. A calibration factor [36] was used to calculate the SENB toughness from the experimental results. The values reported for $\sigma_f$ and $K_{Ic}$ are the average of measurements conducted on 4–6 specimens.

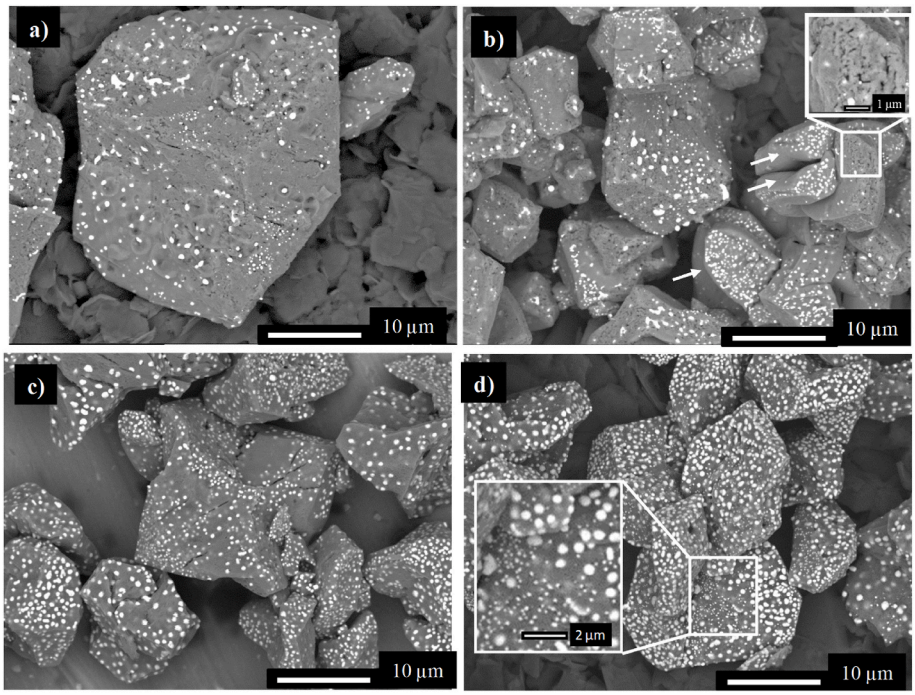


**Fig. 6.** FESEM images of C powders: (a) C23; (b) C31; (c) C52 and (d) C62. The inset in (b) shows the vermicular microstructure of an $Al_2O_3$ grain. The arrows point to grain faces devoid of Fe particles. The inset in (d) shows a grain with a bimodal distribution of the Fe particles.

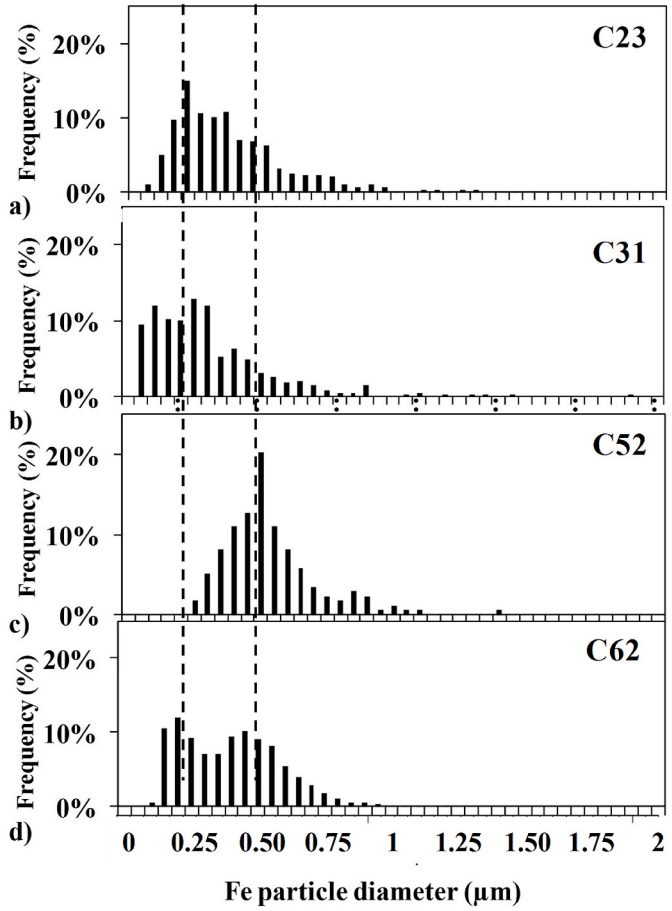


**Fig. 7.** Distribution of the diameter of the Fe particles derived from FESEM images for C powders: (a) C23; (b) C31; (c) C52 and (d) C62. T.

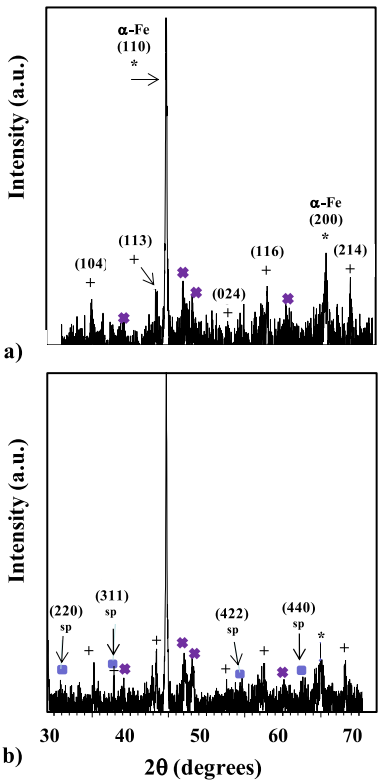


**Fig. 8.** (a) XRD pattern of the polished surface; (b) XRD pattern of the core of the polished cross-section. The peaks of α-Fe (*), α-$Al_2O_3$ (+), $FeAl_2O_4$ spinel (■) and paste (✖) are indicated. The patterns are normalized to the α-Fe (110) peak.

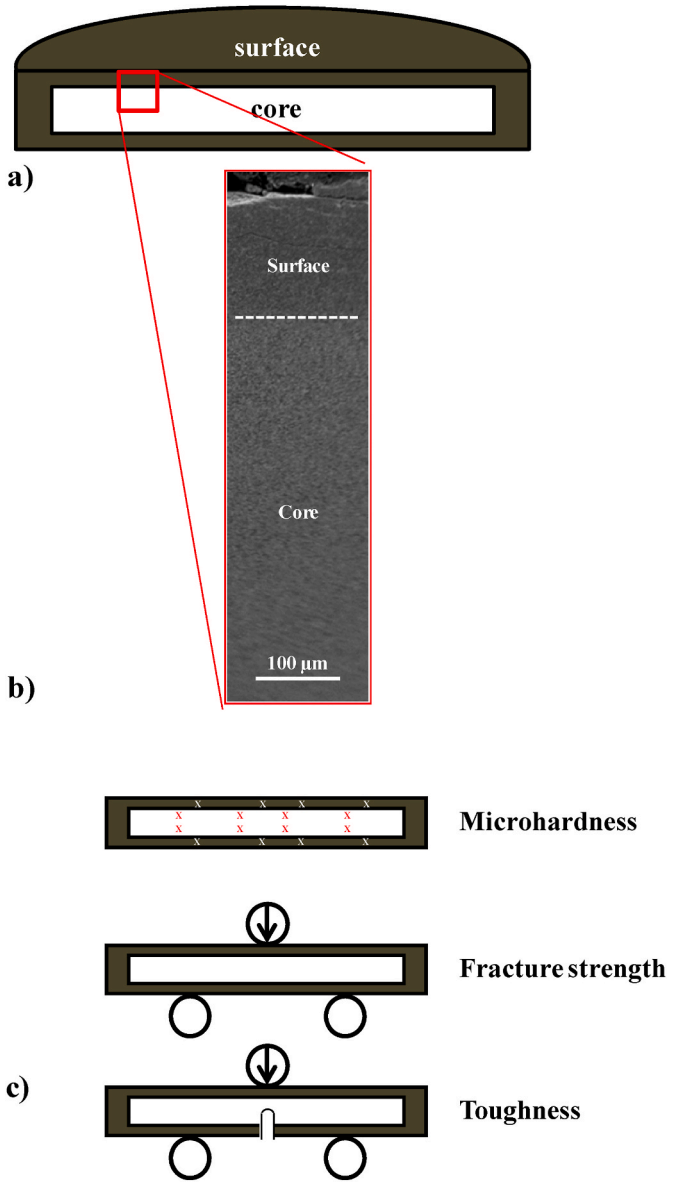


**Fig. 9.** (a) Schematic showing the surface and core microstructure; (b); low-magnification SEM image revealing no Fe gradients on the surface or the core for C52S; (c) Schematics showing how the test are performed on the test specimens (not to scale). See text for details.

## 3. Results

### 3.1. Powders

The proportions of $Fe^{3+}$ relative to all cations, ($Fe^{3+} + Al^{3+}$), in the O powders (Table 1) were calculated from the iron and aluminium contents measured by ICP-MS. For the C powders, the proportions of $Fe^0$ relative to the Fe–$Al_2O_3$ composite (Table 1) were calculated from these data, assuming a total reduction of the iron ions (Equ. 1):

$$(Al_{1-x}Fe_x)_2O_3 + 3x\ H_{2\ (g)} \rightarrow 2x\ Fe + (1-x)\ Al_2O_3 + 3x\ H_2O_{\ (g)} \quad (1)$$

The O powders showed no peaks on the XRD patterns (not shown), indicating that they are amorphous-$(Al_{1-x}Fe_x)_2O_3$ oxides, in agreement with earlier works [33]. Indeed, on the one hand, any free iron oxide (or an iron-rich oxide) would have crystallized as hematite (α-$Fe_2O_3$ or a hematite-rich solid solution) at about 250 °C and on the other hand, it is known [32–34,37], that the $(Al_{1-x}Fe_x)_2O_3$ oxide solid solutions prepared form the decomposition in air of the mixed-oxalates crystallize into the eta (η) form, a defective spinel-phase cubic transition alumina, at a temperature significantly higher than 400 °C. XRD pattern analysis of the C powders (Fig. 3) revealed that the peaks of α-Fe are detected for all of them, the (110) peak being the major peak of all patterns. Peaks accounting for corundum (α-$Al_2O_3$) are detected for C23 and also for C31, with a lower intensity, whereas weak peaks accounting for θ-$Al_2O_3$ are also detected. By contrast, α-$Al_2O_3$ is not detected for C42, C52 and C62, whereas increasingly weaker peaks accounting for a θ- and/or δ-$Al_2O_3$ are observed. These results bring to light a very limited crystallization state of alumina.

The O31 powder was studied by DTA and TGA in flowing $H_2$. The DTA curve (Fig. 4a) shows an intense and complex endothermic peak that could account for some desorption and for the reduction. No exotherm that could account for the "amorphous → θ" or " θ → α" crystallization of alumina is detected, the latter probably because is occurs above 1000 °C, i.e. higher than the maximum temperature investigated in DTA. It is unclear whether the baseline disruption at about 400 °C is related to some physico-chemical event. The TGA curve (Fig. 4b) recorded simultaneously to the above DTA curve, and the corresponding DTG curve, reveal that the weight loss is progressive, occurring in several steps mostly below *ca.* 500 °C. The TGA curve was also recorded separately in much slower heating conditions better suited for the time-separation of the events (Fig. 4c), The calculated derivative (DTG) curve (red in Fig. 4c) show peaks that could account for the desorption (*ca.* 120 °C) and progressive reduction steps (*ca.* 300, 420 and 650 °C).

The C powders were studied by TGA in flowing air in order to fully re-oxidize the Fe particles. The Fe content in the samples was then calculated and therefore the reduction yield of the starting oxide solid solutions was deducted [38]. The shape of the TGA curve and its DTG curve are similar for all samples. Those for C42 are shown in Fig. 5 as an example. The weight gain, corresponding to the oxidation of the Fe particles into α-$Fe_2O_3$, takes place in several ill-separated steps between about 200 and 650 °C, with a peak maximum on the DTG curve at about 510 °C. A comparison with earlier results [38] indicates that this implies that the Fe particles are located on the surface of the $Al_2O_3$ grains, as opposed to being located within the grains, because such intragranular Fe particles would oxidize above 800 °C. A comparison of the experimental and expected weight gains, assuming all iron is oxidized into α-$Fe_2O_3$, gives reduction yields of all starting oxide solid solutions equal to about 98 ± 2 %.

Typical FESEM images (back-scattered electron images in chemical composition mode) of the C powders are shown in Fig. 6. The Fe particles (appearing white on the images) are homogeneously dispersed on the surface of the $Al_2O_3$ polyhedral grains (appearing grey on the images), about tens of micrometers in size. It seems that the size of the $Al_2O_3$ grains decreases for powders, down to about 10 µm, with a higher Fe content (and therefore a lower $Al_2O_3$ content (Table 1). Some areas that could be ascribed to the so-called vermicular microstructure [39] typical of α-$Al_2O_3$ are observed for C23 and C31 (inset in Fig. 6b) but not for the other samples. There are some grains showing faces devoid of Fe particles whereas some others faces are heavily decorated (solid arrows in Fig. 6b). The density of the surface coverage by the Fe particles is noticeably higher upon the increase in Fe content and their size (diameter) seems to be slightly higher too. It is important to note that the formation of very large Fe particles has not taken place and therefore excessive growth on the surface of the $Al_2O_3$ grains can be ruled out. The inset in Fig. 6d shows an area of C62 where the Fe particle size distribution appears to be bimodal. Histograms showing the diameter distribution have been calculated from the measurements of hundreds of such particles on similar images (Fig. 7). The vertical dashed lines in Fig. 7 are guides to the eye for the low- and high-diameter populations of a possible bimodal distribution, centered at about 0.25 and 0.50 µm, respectively, The distributions for C23 and C31 are similar and not too different for C62, with a median size below 0.30 µm, Only C52 shows a monomodal Fe diameter distribution, with only the larger population,

**Table 2**
Characteristics and properties of the sintered specimens: initial Fe content, surface and core Fe contents[a, b, c, d, e, f, g] (see text and Fig. 14), measured density (ρ), relative density (%), surface Vickers microhardness ($HV_{0.5}$) for the surface and core, fracture strength ($\sigma_f$), SENB toughness ($K_{Ic}$).

| Specimen or Ref. | Fe content (vol%) | | | SPS T, P (°C, MPa) | ρ (g.cm$^c$) | d (%) | $HV_{0,5}$ surface (GPa) | $HV_{0,5}$ core (GPa) | $\sigma_f$ (MPa) | $K_{Ic}$ (MPa.m$^{1/2}$) |
|---|---|---|---|---|---|---|---|---|---|---|
| | Initial | Surface | Core | | | | | | | |
| C23S | 14.2 | 16 | 16 | 1400, 50 | 4.46 | 97 | 10.5 ± 0.7 | 9.6 ± 0.3 | 706 ± 124 | 7.7 ± 0.6 |
| C42S | 28.6 | 18 | 24 | 1250, 50 | 4.69 | 96 | 5.2 ± 0.3 | 8.9 ± 0.5 | 937 ± 99 | 8.2 ± 0.7 |
| C52S | 37.4 | 16 | 32 | 1250, 50 | 5.44 | 96 | 6.3 ± 0.7 | 8.5 ± 0.2 | 794 ± 64 | 13.4 ± 0.5 |
| C62S | 47.4 | 18 | 42 | 1250, 50 | 5.57 | 99 | 4.8 ± 0.4 | 6.8 ± 0.8 | 888 ± 88 | 15.2 ± 1.7 |
| [12] [a] | 10 | 10 | 10 | 1450, 43 | – | 99 | – | – | 595 | 6.5 |
| [10] [b] | 20 | 20 | 20 | 1400, 25 | – | – | – | – | – | 10.9 |
| [15] [c] | 20 | 20 | 20 | 1400, 30 | | 97.5 | 11.8 | – | 310 | 10.4 |
| [17] [d] | 20 | 20 | 20 | 1400, 25 | | | | – | 641 | 6.9 |
| [14] [e] | 25 | 25 | 25 | 1700, vac. | 4.89 | – | 4.2 | – | – | 4.97 |
| [13] [f] | 35 | 35 | 35 | 1500, vac. | – | 99 | – | – | 503 | 7.1 |
| [13] [f] | 35 | 35 | 35 | 1500, Ar | – | 99 | – | – | – | 10.2 |
| [11] [g] | 36 | 36 | 36 | 1650, 30 | 5.24 | 97.9 | 6.4 | – | 430 | 7.8 |

[a] Hot-pressing, SENB toughness.
[b] Hot-pressing, double cantilever beam (DCB) toughness.
[c] Reaction sintering, indentation toughness, interconnected network of Fe.
[d] Hot-pressing.
[e] Natural sintering, indentation toughness.
[f] Reaction sintering, indentation toughness, interconnected network of Fe.
[g] Hot-pressing, indentation toughness.

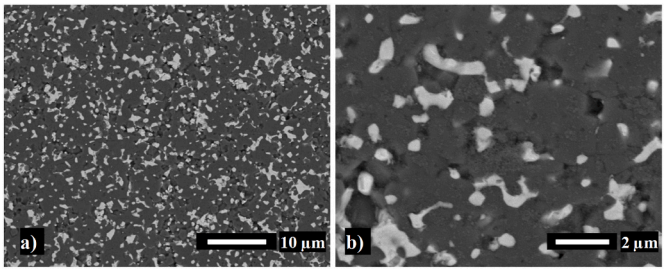


**Fig. 10.** FESEM images of a transverse section of the C23S sample; b) higher-magnification image.

resulting in a higher median size (0.50 µm), Why it is so, or why does C62 show smaller particles than C52, is a complex topic that will be the subject of future works but falls outside of the scope of the present paper. Important points to note then are that these results confirm that the Fe particles diameter is below 1 µm and that the formation of larger ones has not taken place even for samples with as much as 47 vol% Fe.

### 3.2. Sintered sample

XRD pattern analysis of the polished surface of the sintered samples revealed peaks accounting for α-Fe and α-$Al_2O_3$ (Fig. 8a). Weak peaks accounting for the spinel $FeAl_2O_4$ are also detected in the XRD patterns of the core of the polished cross-section (Fig. 8b). Indeed, cutting the samples to prepare test speciments revealed that all samples with a higher Fe content than C23S, which exhibits a homogeneous microstructure, display a surface/core microstructure (schematic in Fig. 9a). $FeAl_2O_4$ could have been formed by oxidation of the Fe particles when the amorphous $Al_2O_3$ crystallized into transition- and α-$Al_2O_3$ during SPS, favored by the exothermicity of the crystallization and the corresponding widespread crystalline rearrangements, notably for the anionic ($O^{2-}$ ions) sub-lattice. FESEM images confirm that except for C23S, the samples show a surface/core microstructure. The thickness of the surface layer is equal to 150–200 µm for C42S, C52S and C62S. It is similar at the top and bottom of the pellet. Low-magnification SEM images such as the one shown in Fig. 9b revealed no Fe gradients on the surface or the core of the specimens. The measured density (ρ - Table 2) increases upon the increase in Fe content. The relative density (d - Table 2) was estimated using the proportions of the different compounds detected in the core of the samples, as detailed later in the text. It is in the range 96–99 %.

A series of FESEM images (Fig. 10, Fig. 11, Fig. 12, Fig. 13) showing a transverse section of the samples are presented. For C23S (Fig. 10), as mentioned above, the sample is homogeneous. For C42S (Fig. 11a and b), C52S (Fig. 12a and b) and C62S (Fig. 13a and b), the surface looks similar to that of C23S. The size of the Fe particles in the surface was evaluated on similar images. The Fe particles are smaller than about 2 µm and $d_{50}$ is equal to 0.44, 0.39, 0.44 and 0.47 for CS23S, CS42S, CS52S and CS62S, respectively. By contrast, for the core of C42S (Fig. 11c and d), C52S (Fig. 12c and d) and C62S (Fig. 13c and d), the proportion of metallic phase (appearing white on the images) appears to increase upon the increase of iron in the samples. For C42S, the core Fe particles (about 1–2 µm) are larger than the surface particles but for C52S and C62S, it has not been possible to determine individual particle sizes because Fe forms a continuous, percolating, network. Some spinel ($FeAl_2O_4$) grains are also observed in the cores (yellow arrows in Fig. 11d, 12d and 13d). Their size is no more than 1 µm for C42S and no more than 0.5 µm for C52S and C62S. The size of the $Al_2O_3$ grains is in the range 1–3 µm for CS23, and about 1 µm for C42S, C52S and C62S. These results indicate that the Fe content in the core increases for the series of samples, as expected, but that it does not for the surface. Image analysis of similar FESEM images, with three compounds (Fe, $FeAl_2O_4$ and $Al_2O_3$), revealed (Fig. 14) that the cores are of the desired Fe–$Al_2O_3$ composition (along with some $FeAl_2O_4$), whereas the surface iron content is about 16 vol% for all samples. This could indicate that some iron has left the sample during SPS for C42S, C52S and C62S and indeed some solidified Fe droplets have been observed outside the die near the surrounding graphite paper. As it is generally accepted that the temperature of the sample inside the mould is often higher than at its outer periphery where the pyrometer measures it, especially for electrically conducting materials [40–42]. As C42S, C52S and C62S are close or above the electrical percolation threshold, we propose that this could reflect the melting of some Fe particles which would have been driven out of the die owing to the uniaxial pressure applied during the SPS. By contrast, it is proposed that C23S shows a negligible electrical conductivity and that the SPS current lines thus flow in the carbon stack, as opposed to through the specimen, and therefore there is no marked temperature increase within the sample where the Fe particles did not melt. Guichard et al. [11] also observed in iron-depleted surface for Fe–$Al_2O_3$ samples prepared by hot-pressing. By contrast to the present results, these authors observed that the thickness of the surface layer increased up to

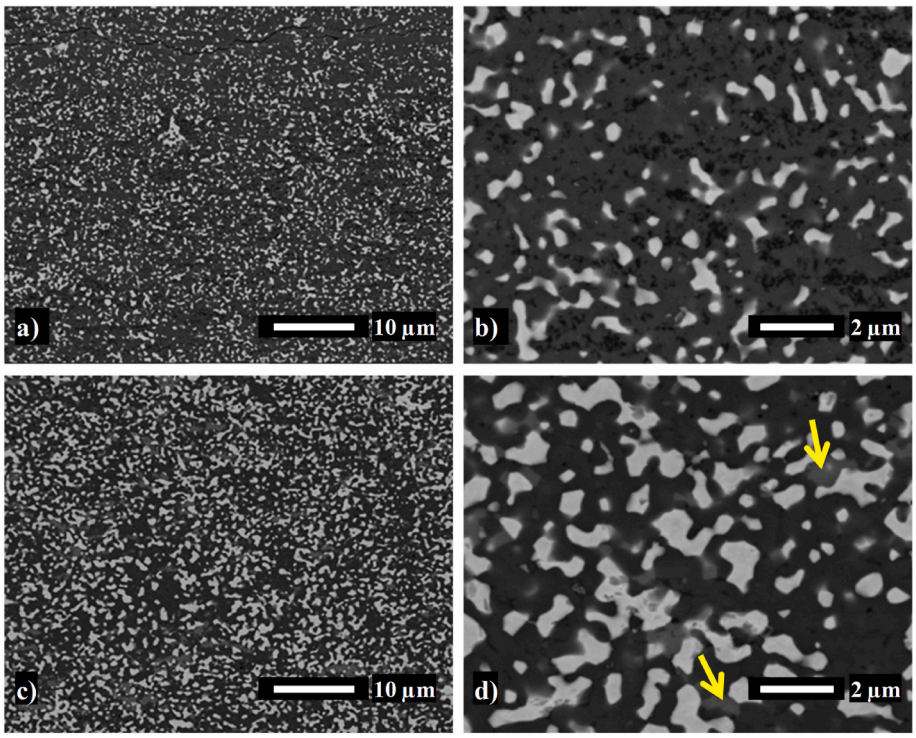


**Fig. 11.** FESEM images of a transverse section of the C42S sample: a) surface; c) core. b) and d) are higher-magnification images of a) and c), respectively. The arrows point to $FeAl_2O_4$ grains (appearing grey on the image).

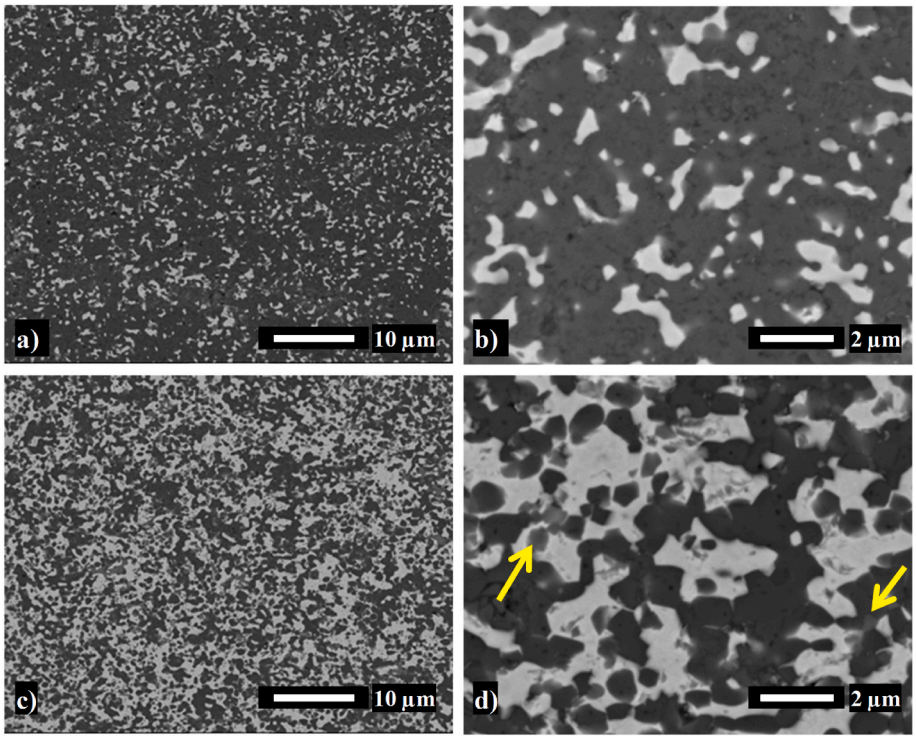


**Fig. 12.** FESEM images of a transverse section of the C45S sample: a) surface; c) core. b) and d) are higher-magnification images of a) and c), respectively. The arrows point to $FeAl_2O_4$ grains (appearing grey on the image).

about 200 µm upon the increase in total metal content. They proposed that graphite from the die lining diffuses into the sample and combines with iron to form cast iron which melts and exudes under the uniaxial pressure.

The way the specimens were tested for microhardness, fracture strength and toughness is schematized in Fig. 9c. The Vickers microhardness for the surface of the samples (Table 2), measured on cross-sections of the specimens, is equal to 10.5 GPa for C23S and to 4.8–6.3 GPa for the C42S, C52S and C62S. The higher value for C23S could be consequence of a slightly higher density and a SPS temperature

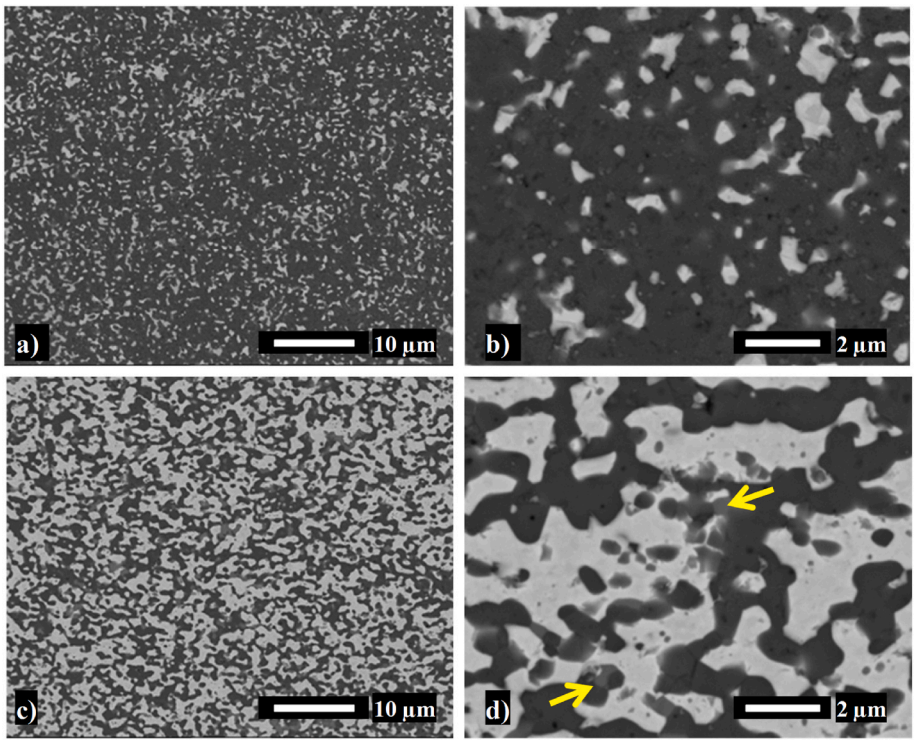


**Fig. 13.** FESEM images of a transverse section of the C62S sample: a) surface; c) core. b) and d) are higher-magnification images of a) and c), respectively. The arrows point to $FeAl_2O_4$ grains (appearing grey on the image).

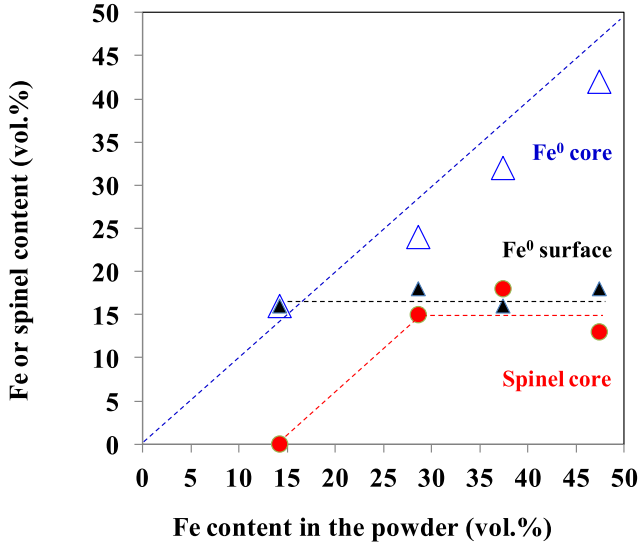


**Fig. 14.** Fe and spinel content (vol%) in the dense samples (surface and core) as deduced from FESEM image analysis versus the Fe content in the powders. (△) $Fe^0$ core; (▲) $Fe^0$ surface; (●) spinel core. The dashed line are guides to the eye. See text for details.

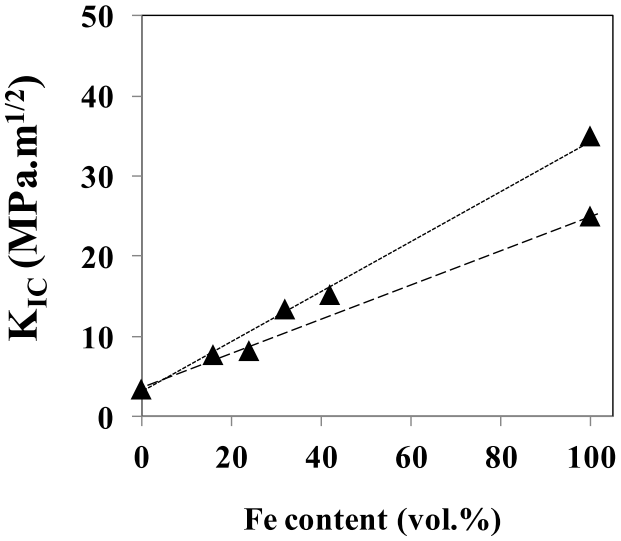


**Fig. 15.** Toughness values for the present samples and common values for $Al_2O_3$ (3.4 MPa $m^{1/2}$) and Fe (25 or 35 MPa $m^{1/2}$) showing a rule-of-mixture behavior.

of 1400 °C *vs* 1250 °C. For the core, it is equal to 9.6, 8.9, 8.5 and 6.8 GPa for C23S,42S, C52S and C62S, respectively, showing a progressive decrease upon the increase in Fe content. The transverse fracture strength ($\sigma_f$ - Table 2) values show a fairly high dispersion. The average value is close to 700 MPa for C23S, the sample with the lower initial Fe content and the only one with no surface/core microstructure, whereas it is in the range 800–1000 MPa for C42S, C52S and C62S. It is thought that the surface layer thickness is high enough (150–200 µm), above the critical flaw size, evaluated in the range 25–90 µm for Fe–$Al_2O_3$ composites [11], for the test to be representative of the surface, not the core (Fig. 9c). Therefore a similar value for C42S, C52S and C62S is in line with a similar Fe surface content and $Al_2O_3$ matrix grain size, whereas the slightly lower fracture strength for C23S would reflect the higher $Al_2O_3$ matrix grain size (1–3 µm vs 1 µm). The toughness ($K_{Ic}$ - Table 2) is in the range 7.7–15.7 MPa $m^{1/2}$. The notch depth (>720 µm) is sufficient to reach the core of the samples and therefore the values are characteristic of the core, not the surface. It is important to note that the toughness is about 8 MPa $m^{1/2}$ for the samples showing discrete core Fe particles (C23S and C42S), whereas it is noticeably higher, about 14

MPa $m^{1/2}$, for the samples showing a continuous Fe network (C52S and C62S). Interestingly, plotting the present toughness data and common values found for $Al_2O_3$ (3.4 MPa $m^{1/2}$) and Fe (25 or 35 MPa $m^{1/2}$) show a rule-of-mixture behavior (Fig. 15). As mentioned above, there is no marked difference in the $Al_2O_3$ grain size for C42S, C52S and C62S and therefore this parameter should not play a role in the observed toughness increase. It is not within the scope of this work to go into the details of the toughening mechanism but, following other authors [10–15,17], toughening is attributed to a combination of crack-bridging and crack-deflection by the ductile metallic phase. Interestingly, the latter values are higher than those reported by other authors [13,15] for Fe–$Al_2O_3$ composites showing an interconnected network of Fe, just above 10 MPa $m^{1/2}$ [Table 2] as deduced from indentation data, moreover using a method often considered to overestimate toughness. The present results could arise from a higher degree of uniformity of the continuous Fe network, itself arising from the very homogeneous distribution of submicrometer-size Fe particles in the corresponding powders.

## 4. Conclusions

Fe–$Al_2O_3$ composite powders with relatively high metal contents (14.2–47.4 vol%) were prepared by selective reduction in $H_2$ of the corresponding amorphous $Al_{2-2x}Fe_{2x}O_3$ solid solutions. The density of Fe particles at the surface of the $Al_2O_3$ grains strongly increases upon the increase in iron content but it is shown that they do not coalesce and remain submicrometer-sized, even for the higher Fe contents,. The details of the formation of the Fe particles and the limitation of the crystallization of alumina to the δ and θ forms, as opposed to the α form, warrant further studies. The dense samples prepared by SPS tend to show a surface/core microstructure. For all samples, the surface, about 150–200 μm thick, contains about only 16 vol% Fe dispersed as discrete particles smaller than 0.5 μm in size. This could reflect that melted Fe particles are driven out of the die owing to the uniaxial pressure, despite the relatively moderate SPS temperate (1250 °C). It is further shown that Fe forms a continuous percolating network for the samples with the higher content Fe in the core (32 and 42 vol%), as opposed to discrete particles for the other samples (16 and 24 vol%). This accounts for a significantly higher toughness for the former than for the latter samples (about 14 and 8 MPa $m^{1/2}$, respectively). Thus, it is shown that despite the high Fe content, a preparation way has been found that avoids the excessive growth of the Fe particles and the resulting poorly homogeneous microstructure, and that by contrast the very homogeneous Fe interconnected network provides extra toughening. The electromagnetic properties of similar samples will be the subjet of future studies.

## Declaration of competing interest

The authors declare that they have no known competing financial interests or personal relationships that could have appeared to influence the work reported in this paper.

## Acknowledgments

The SPS was performed at the Plateforme Nationale CNRS de Frittage-Flash (PNF$^2$, Toulouse), electron microscopy was performed at Centre de microcaractérisation Raimond Castaing - UAR 3623 (Toulouse).

## References

[1] J.A. Yeomans, Ductile particle ceramic matrix composites - scientific curiosities or engineering materials? J. Eur. Ceram. Soc. 28 (2008) 1543–1550.
[2] T. Rodriguez-Suarez, J.F. Bartolomé, J.S. Moya, Mechanical and tribological properties of ceramic/metal composites: a review of phenomena spanning from the nanometer to the micrometer length scale, J. Eur. Ceram. Soc. 32 (2012) 3887–3898.
[3] L.S. Sigl, P.A. Mataga, B.J. Dalgleish, R.M. McMeeking, A.G. Evans, On the toughness of brittle materials reinforced with a ductile phase, Acta Metall. 36 (1988) 945–953.
[4] F. Erdogan, P.F. Joseph, Toughening of ceramics through crack bridging by ductile particles, J. Am. Ceram. Soc. 72 (1989) 262–270.
[5] P.F. Becher, Microstructural design of toughened ceramics, J. Am. Ceram. Soc. 74 (1991) 255–269.
[6] K.S. Ravichandran, The mechanics of toughness development in ductile phase reinforced brittle matrix composites, Acta Metall. Mater. 40 (1992) 1009–1022.
[7] C.O. McHugh, T.J. Whalen, M. Humenik Jr., J. Am. Ceram. Soc. 49 (1966) 486–491.
[8] X. Devaux, Ch Laurent, M. Brieu, A. Rousset, Propriétés microstructurales et mécaniques de nanocomposites à matrice céramique, C. R. Acad. Sci. Paris Série II 312 (1991) 1425–1430.
[9] P. Matteazzi, G. Le Caër, Synthesis of nanocrystalline alumina-metal composites by room-temperature ball-milling of metal oxides and aluminum, J. Am. Ceram. Soc. 75 (1992) 2749–2755.
[10] P.A. Trusty, J.A. Yeomans, The toughening of alumina with iron: effects of iron distribution on fracture toughness, J. Eur. Ceram. Soc. 17 (1997) 495–504.
[11] J.-L. Guichard, O. Tillement, A. Mocellin, Preparation and characterization of alumina–iron cermets by hot-pressing of nanocomposite powders, J. Mater. Sci. 32 (1997) 4513–4521, https://doi.org/10.1023/A:1018665116215.
[12] Ch Laurent, A. Peigney, O. Quénard, A. Rousset, Synthesis and mechanical properties of nanometric metal particles-ceramic matrix nanocomposites, Silic. Ind. 63 (1998) 77–84.
[13] S. Schicker, T. Erny, D.E. Garcia, R. Janssen, N. Claussen, Microstructure and mechanical properties of Al-assisted sintered Fe/$Al_2O_3$ cermets, J. Eur. Ceram. Soc. 19 (1999) 2455–2463.
[14] K. Konopka, A. Oziebło, Microstructure and the fracture toughness of the $Al_2O_3$-Fe composites, Mater. Char. 46 (2001) 125–129.
[15] M.M. El-Sayed Seleman, X. Sun, L. Zuo, Effect of iron morphology and interfacial bonding on the toughening of $Al_2O_3$/Fe composites, J. Mater. Sci. Technol. 17 (2001) S47–S51.
[16] M. Aldridge, J.A. Yeomans, The Thermal shock behavior of ductile particle toughened alumina, J. Eur. Ceram. Soc. 19 (1999) 1769–1775.
[17] M. Aldridge, J.A. Yeomans, Thermal shock behavior of iron-particle-toughened alumina, J. Am. Ceram. Soc. 84 (2001) 603–607.
[18] O.L. Ighodaro, O.I. Okoli, Fracture toughness enhancement for alumina Systems: a review, Int. J. Appl. Ceram. Technol. 5 (2008) 313–323. https://doi.org/10.4028/www.scientific.net/MSF.706-709.1984.
[19] J. Gurt Santanach, C. Estournès, A. Weibel, A. Peigney, G. Chevallier, Ch Laurent, Spark plasma sintering as a reactive sintering tool for the preparation of surface-tailored Fe–Fe$Al_2O_4$-$Al_2O_3$ nanocomposites, Scripta Mater. 60 (2009) 195–198, https://doi.org/10.1016/j.scriptamat.2008.09.034.
[20] K.R. Ravi, A. Murugesan, V. Udhayabanu, R. Subramanian, B.S. Murty, Microstructure and mechanical property of Fe-$Al_2O_3$ nanocomposites synthesized by reactive milling followed by spark plasma sintering, Mater. Sci. Forum 710 (2012) 291–296.
[21] M. Nanko, D. Maruoka, N.D. Thuy, Multi-functional metal/ceramic hybrid composites for structural applications, Mater. Sci. Forum 706–709 (2012) 1984–1989.
[22] A. Marchand, B. Barbara, P. Mollard, G. Fillion, X. Devaux, A. Rousset, On a series of nanoparticles of iron epitaxed on $Al_2O_3$: a new field, temperature and concentration (of Fe) scaling plot of the magnetization curves, J. Magn. Magn Mater. 116 (1992) 64–66.
[23] M. Pardavi-Horvath, L. Takacs, Iron-alumina nanocomposites prepared by ball milling, IEEE Trans. Magn. 28 (1992) 3186–3188.
[24] T. Ambrose, A. Gavrin, C.L. Chien, Formation and magnetic properties of nanocomposite Fe-$Al_2O_3$ using high-energy ball milling, J. Magn. Magn Mater. 116 (1992) L311–L314.
[25] A. Marchand, X. Devaux, B. Barbara, P. Mollard, M. Brieu, A. Rousset, Microstructural and magnetic characterization of alumina-iron nanocomposites, J. Mater. Sci. 28 (1993) 2217–2226.
[26] Z. Zhang, R. Fan, Z. Shi, S. Pan, K. Yan, K. Sun, J. Zhang, X. Liu, X. Wang, S. Dou, Tunable negative permittivity behavior and conductor–insulator transition in dual composites prepared by selective reduction reaction, J. Mater. Chem. C 1 (2013) 79–85, https://doi.org/10.1039/c2tc00269h.
[27] Z. Zhang, R. Fan, Z. Shi, K. Yan, Z. Zhang, X. Wang, S. Dou, Microstructure and metal-dielectric transition behaviour in a percolative $Al_2O_3$-Fe composite via selective reduction, RSC Adv. 3 (2013) 26110–26115, https://doi.org/10.1039/c3ra45253k.
[28] Z. Shi, R. Fan, K. Yan, K. Sun, M. Zhang, C. Wang, X. Liu, X. Zhang, Preparation of iron networks hosted in porous alumina with tunable negative permittivity and permeability, Adv. Funct. Mater. 23 (2013) 4123–4132, https://doi.org/10.1002/adfm.201202895.
[29] K. Sun, H. Fan, Z.D. Zhang, K.L. Yan, X.H. Zhang, P.T. Xie, M.X. Yu, S.B. Pan, The tunable negative permittivity and negative permeability of percolative Fe/Al2O3 composites in radio frequency range, Appl. Phys. Lett. 106 (2015), 172902, https://doi.org/10.1063/1.4918998.
[30] R.A. Raimundo, R.S.S. Reinaldo, N.T. Câmara, C.S. Lourenço, F.A. Costa, D. A. Macedo, U.U. Gomes, M.A. Morales, $Al_2O_3$-10 wt% Fe composite prepared by high energy ball milling: structure and magnetic properties, Ceram. Int. 47 (2021) 984–991, https://doi.org/10.1016/j.ceramint.2020.08.212.
[31] M.F. Ashby, F.J. Blunt, M. Bannister, Flow characteristics of highly constrained metal wires, Acta Metall. 37 (1989) 184–18577.

[32] X. Devaux, Ch Laurent, A. Rousset, Chemical synthesis of metal nanoparticles dispersed in alumina, Nanostruct. Mater. 2 (1993) 339–346.
[33] A. Rousset, J. Pâris, Formation de solutions solides binaires et ternaires des sesquioxydes de chrome, d'aluminium et de fer. III - Le système $Fe_2O_3$-$Al_2O_3$, Bull. Soc. Chim. 10 (1972) 3729–3733.
[34] X. Devaux, Ch Laurent, M. Brieu, A. Rousset, Iron-alumina interface in ceramic matrix nanocomposites, J. All. Cpds 188 (1992) 179–181 179.
[35] Ch Laurent, A. Rousset, M. Verelst, K.R. Kannan, A.R. Raju, C.N.R. Rao, Reduction behaviour of $Fe^{3+}/Al_2O_3$ obtained from the mixed oxalate precursor and the formation of the $Fe^0$-$Al_2O_3$ metal-ceramic composite, J. Mater. Chem. 3 (1993) 513–518.
[36] W.F. Brown, J.E. Srawley, Plane Strain Crack Toughness Testing of High Strength Metallic Materials, American Society For Testing And Materials, Philadelphia, PA (USA), 1966.
[37] A. Polli, F.F. Lange, C.G. Levi, J. Mayer, Crystallisation behavior and microstructure evolution of $(Al, Fe)_2O_3$ synthezed from liquid precursors, J. Am. Ceram. Soc. 79 (1996) 1745–1755.
[38] Ch Laurent, Ch Blaszczyk, M. Brieu, A. Rousset Elaboration, Microstructure and oxidation behavior of metal-alumina and metal-chromia nanocomposite powders, Nanostruct. Mater. 6 (1–4) (1995) 317–320.
[39] J.L. McArdle, G.L. Messing, Seeding with γ-alumina for transformation and icrostructure control in boehmite-derived α-alumina, J. Am. Ceram. Soc. 69 (5) (1986). C-98-C-101.
[40] C. Arnaud, C. Manière, G. Chevallier, C. Estournès, R. Mainguy, F. Lecouturier, D. Mesguich, A. Weibel, L. Durand, C. Laurent, Dog-bone copper specimens prepared by one-step spark plasma sintering, J. Mater. Sci. 50 (2015) 7364–7373, https://doi.org/10.1007/s10853-015-9293-5.
[41] C. Manière, A. Pavia, L. Durand, G. Chevalier, K. Afanga, C. Estournès, Finite-element modeling of the electro-thermal contacts in the Spark Plasma Sintering process, J. Eur. Ceram. Soc. 36 (2016) 741–748, https://doi.org/10.1016/j.jeurceramsoc.2015.10.033.
[42] C. Manière, L. Durand, E. Brisson, H. Desplats, P. Carré, P. Rogeon, C. Estournès, Contact resistances in spark plasma sintering: from in-situ and ex-situ determinations to an extended model for the scale up of the process, J. Eur. Ceram. Soc. 37 (2017) 1593–1605, https://doi.org/10.1016/j.jeurceramsoc.2016.12.010.